JACS
JOURNAL OF THE AMERICAN CHEMICAL SOCIETY
pubs.acs.org/JACS
Article

Generation and Aerobic Oxidative Catalysis of a Cu(II) Superoxo Complex Supported by a Redox-Active Ligand

Maia E. Czaikowski, Andrew J. McNeece, Jan-Niklas Boyn, Kate A. Jesse, Sophie W. Anferov, Alexander S. Filatov, David A. Mazziotti, and John S. Anderson*

Cite This: J. Am. Chem. Soc. 2022, 144, 15569−15580
Read Online
ACCESS | Metrics & More | Article Recommendations | Supporting Information

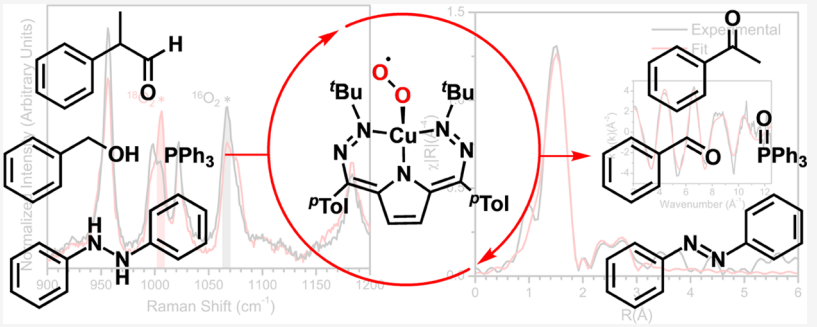

ABSTRACT: Cu systems feature prominently in aerobic oxidative catalysis in both biology and synthetic chemistry. Metal ligand cooperativity is a common theme in both areas as exemplified by galactose oxidase and by aminoxyl radicals in alcohol oxidations. This has motivated investigations into the aerobic chemistry of Cu and specifically the isolation and study of Cu−superoxo species that are invoked as key catalytic intermediates. While several examples of complexes that model biologically relevant Cu(II) superoxo intermediates have been reported, they are not typically competent aerobic catalysts. Here, we report a new Cu complex of the redox-active ligand ^{tBu,Tol}DHP (2,5-bis((2-*t*-butylhydrazono)(*p*-tolyl)methyl)-pyrrole) that activates O_2 to generate a catalytically active Cu(II)-superoxo complex via ligand-based electron transfer. Characterization using ultraviolet (UV)−visible spectroscopy, Raman isotope labeling studies, and Cu extended X-ray absorption fine structure (EXAFS) analysis confirms the assignment of an end-on κ^1 superoxo complex. This Cu−O_2 complex engages in a range of aerobic catalytic oxidations with substrates including alcohols and aldehydes. These results demonstrate that bioinspired Cu systems can not only model important bioinorganic intermediates but can also mediate and provide mechanistic insight into aerobic oxidative transformations.

INTRODUCTION

Dioxygen is an abundant, inexpensive, atom-economical, and environmentally benign oxidant compared to widely used stoichiometric reagents such as chromium and manganese oxides, peracids, and hypervalent iodine species.[1−11] Nevertheless, implementing O_2 in a catalytic regime requires mechanistic control over its kinetically unfavorable activation and overoxidation of substrates. Copper-based systems, particularly those coupled with redox-active additives such as aminoxyl radicals, have emerged as effective catalysts for aerobic oxidations (Figure 1A).[12−26] Enabled by Cu's accessible redox chemistry, facile ligand exchange, and broad functional group compatibility, synthetic C−H functionalization methods have been developed to access two-electron processes, especially when combined with co-catalysts.[27−31]

The efficacy of Cu in aerobic oxidation chemistry is in large part motivated by its prevalence in biological oxidations.[32] This prevalence has spurred efforts to synthesize compounds that model the active sites of Cu-containing monooxygenase and oxidase metalloproteins (Figure 1B). Efforts over many years have successfully isolated examples of several oxygenated Cu intermediates such as mononuclear Cu−superoxo species.[20,22−24,33−42] While synthetic Cu(II)-superoxo complexes have been characterized,[35−37,40,41] well-characterized end-on examples in a monooxygenase-like N3 T-shaped ligand geometry are comparatively rare.[24,38,43] These bioinspired Cu systems have also been applied to alcohol oxidation and hydroxylation reactivity, but in these cases, thorough observation or characterization of discrete intermediates, such as Cu−superoxo complexes, is often not possible; detailed characterization of unifying intermediates such as Cu−superoxo complexes is lacking generally for catalytic

Received: April 29, 2022
Published: August 17, 2022

https://doi.org/10.1021/jacs.2c04630
J. Am. Chem. Soc. 2022, 144, 15569−15580

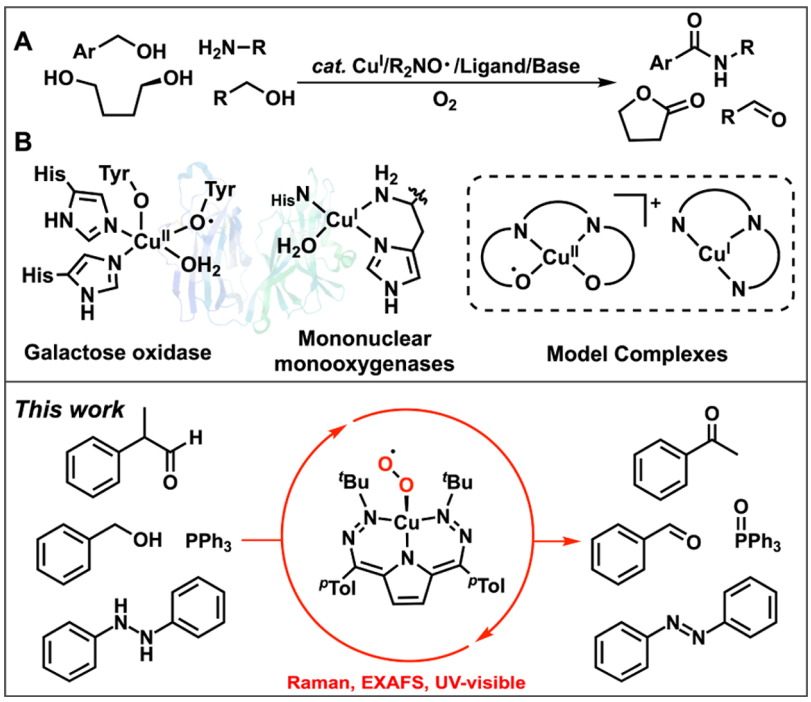

Figure 1. Overview of representative (A) Cu(I) + aminoxyl catalysts for aerobic oxidations, (B) general model compound structures based on Cu monooxygenase and oxidase active sites and this work: a bioinspired Cu(II) aerobic oxidation catalyst with a well-characterized Cu−superoxo intermediate.

systems.[17,18,24,44] Thus, while enzyme model complexes enable the isolation of putative catalytic intermediates, these model systems are typically not competent catalysts. In support of this scarcity, there has been only one example of a catalytic transformation mediated by a well-characterized Cu−superoxo complex, and we note that this example is a redox-neutral aldol coupling.[43] Conversely, thoroughly characterized superoxo intermediates in aerobic catalysis have been observed in Mn-, Fe-, and Co-based systems, which makes the rarity of similarly observable species in the ubiquitous aerobic catalysis of Cu even more notable.[45−48]

We have recently been interested in using biomimetic approaches with dihydrazonopyrrole (DHP) ligand scaffolds that can support H^+, e^-, H-atom, or H_2 transfer similar to biological cofactors or active sites. This strategy has enabled the generation of superoxo and hydroperoxo intermediates with Ni and Fe, respectively,[49,50] but no aerobic catalysis was observed in these systems. We rationalized that the noted aerobic chemistry of Cu might enable oxidative catalysis and that the established redox activity of the DHP ligand might facilitate the observation and characterization of catalytic intermediates such as superoxo complexes. Here, we demonstrate the success of this strategy with the thorough characterization of a Cu−superoxo intermediate, which notably engages in aerobic catalysis at room temperature with a variety of substrates (Figure 1). These results further underscore how biomimetic approaches can facilitate aerobic catalysis and provide insights into the possible agency of oxygenated Cu intermediates such as superoxo and hydroperoxo species as active oxidants.

RESULTS AND DISCUSSION

Synthesis and Electronic Structures of 1 and 2. Deprotonation of the previously reported dihydrazonopyrrole proligand ^{tBu,Tol}DHP•2 HCl with 4 equiv of *n*-BuLi and 0.5 eq. 1-hexene followed by addition to $CuCl_2$ yields [^{tBu,Tol}DHP$^{2-•}$]-Cu (**1**) as a deep blue complex in 37% yield (Scheme 1).[50]

Scheme 1. Syntheses of 1, 2, and 3

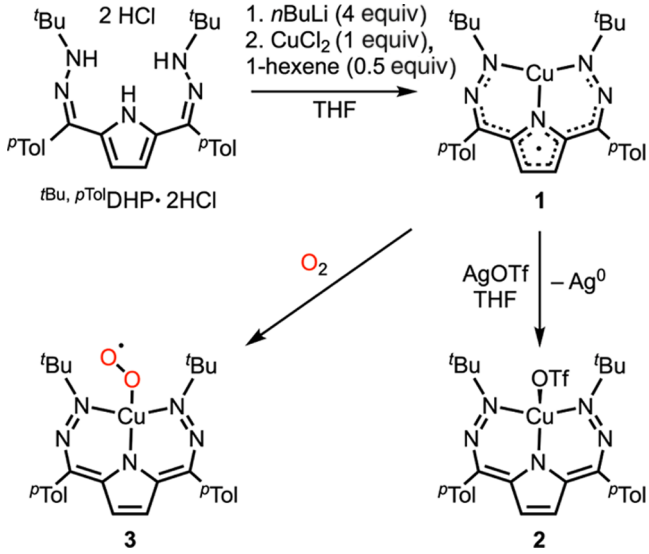

Single-crystal X-ray diffraction (SXRD) reveals a T-shaped complex with Cu−N1/N5 bond lengths of 1.895(3) and 1.890(3) Å and N3−Cu−N5/N1 bond angles of 93.83(1) and 93.66(1)° (Figure 2A). Complex **1** is diamagnetic (Figure S1), but ligand-based redox events previously characterized for [^{tBu,Tol}DHP$^{2-•}$]Ni raise the possibility of an antiferromagnetically coupled (DHP$^{2-•}$)Cu(II) electronic description for **1** rather than a d^{10} (DHP$^-$)Cu(I) complex.[47,50,51] The cyclic voltammogram (CV) of **1** shows three reversible redox

https://doi.org/10.1021/jacs.2c04630
J. Am. Chem. Soc. 2022, 144, 15569−15580

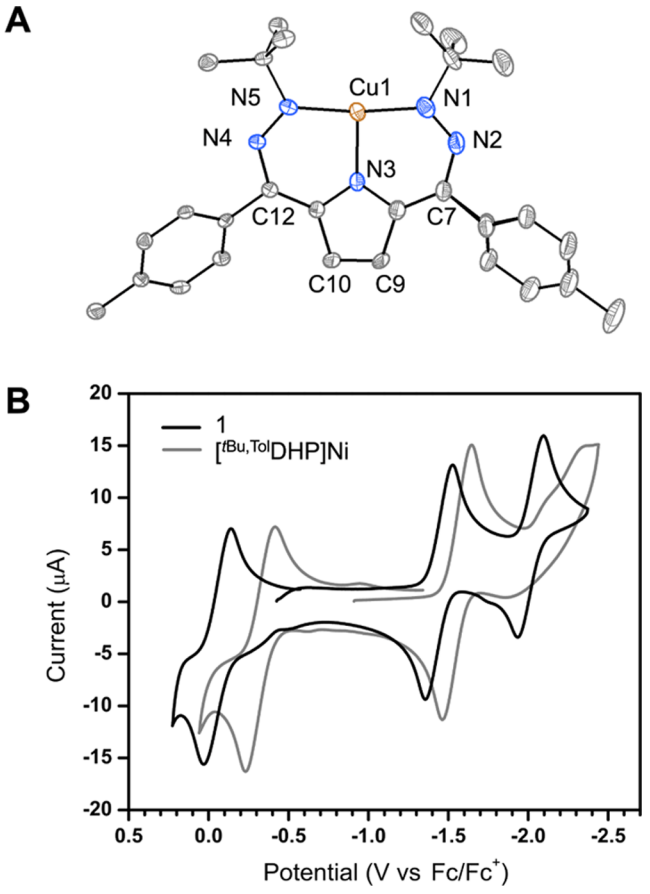

Figure 2. (A) SXRD of **1**. Ellipsoids are set to 50% probability and hydrogen atoms have been omitted for clarity. Selected bond lengths and angles: Cu1−N1 1.895(3) Å, Cu1−N3 1.952(3) Å, Cu1−N5 1.890(3) Å, N1−N2 1.289(3) Å, N5−N4 1.293(4) Å, C9−C10 1.347(5) Å, N1−Cu1−N3 93.66(1)°, and N5−Cu1−N3 93.83(1)°. (B) Cyclic voltammogram of **1** (black line) and [^{tBu,Tol}DHP$^{\bullet}$]Ni (gray line) in THF (1 mM [Cu] or [Ni], 0.1 M NBu_4PF_6, scan rate 100 mV s^{-1}). The small shoulder at −0.3 V for **1** arises from a small impurity in the electrolyte (Figure S29).

features: an oxidation at −0.05 and reductions at −1.45 and −2.03 V versus Fc/Fc^+ (Figure 2B, black). Based on the observed features for [^{tBu,Tol}DHP$^{2-\bullet}$]Ni (Figure 2B, gray) and a putative Cu(II)/DHP$^{2-\bullet}$ electronic structure for **1** (see below), these three features can be tentatively assigned as the (DHP$^-$)Cu(II)/(DHP$^{2-\bullet}$)Cu(II), (DHP$^{2-\bullet}$)Cu(II)/(DHP^{3-})Cu(II), and (DHP^{3-})Cu(II)/(DHP^{3-})Cu(I) couples, respectively. The oxidative feature at −5 mV is shifted 250 mV more positive compared to [^{tBu,Tol}DHP$^{2-\bullet}$]Ni, which demonstrates that the Cu system is more oxidizing.

Based on this electrochemical data, we chemically oxidized **1** with 1.1 equiv of AgOTf, resulting in an immediate color change from blue to green and formation of [^{tBu,Tol}DHP$^-$]CuOTf (**2**) (Scheme 1). The SXRD structure for **2** shows a Cu−OTf bond length of 2.076(2) Å and a distorted tetrahedral geometry with τ_4 and τ_4' values of 0.49 and 0.50, respectively (Figure S43). Complex **2** has broad ^{1}H NMR resonances typical of a paramagnetic Cu(II) center. Evans method analysis provides a μ_{eff} of 1.72 μ_B, which is consistent with an S = 1/2 spin state (spin only: 1.73 μ_B) (Figure S3). The X-band electron paramagnetic resonance (EPR) spectrum of **2** in 1:1 toluene/methylene chloride is consistent with this assignment, with a near-axial signal at g = 2.063, 2.064, and 2.083 (Figure S19). The ^{19}F NMR signal for **2** is broadened and shifted compared to free triflate consistent with some solution state anion binding (Figure S4). Changes to the DHP bond lengths upon oxidation of **1** to **2** support that ligand-based oxidation may be occurring. Notably, the shortening of the N1−N2/N5−N4 hydrazone arms and C9−C10 pyrrole backbone bond lengths matches a simplistic resonance description of the expected bond contractions upon oxidation of the radical dianion ligand to the monoanion (Table S19). Nevertheless, we wanted to obtain additional support for this (DHP$^{2-\bullet}$)Cu(II) electronic structure assignment.

We acquired Cu K-edge X-ray absorption spectroscopy (XAS) spectra of **1** and **2** to further probe the geometry and proposed electronic structures using **2** as a bonafide Cu(II) reference complex (Figure 3A). Complex **1** has an intense rising-edge feature at 8982.5 eV, which we assign as a shakedown 1s → 4p transition with a simultaneous ligand-to-metal charge-transfer excitation by analogy to the same feature observed in the isostructural complex [^{tBu,Tol}DHP$^{2-\bullet}$]Ni.[50] Similar rising-edge shakedown features are observed for Cu(II) complexes, which supports our assignment of a (DHP$^{2-\bullet}$)Cu(II) electronic structure; however, we note that rising-edge features are also observed for Cu(I) complexes, which convolutes this assignment.[52−55]

The energy of the 1s → 4p transition for **1** is lower than that for square planar Cu(II) complexes, which may reflect that the open coordination site trans to the pyrrole for this T-shaped complex stabilizes the 4p$_x$ orbital and shifts the transition to lower energy.[56−60] Related rising-edge features have also been associated with some T-shaped Cu(I) complexes, where the electric dipole-allowed 1s → 4p transition corresponds to a sharp rising-edge peak, although such peaks are typically of a larger normalized intensity than what is observed for **1**.[61,62] In addition to the rising-edge feature, there is a notable absence of a pre-edge feature, which might be expected for a Cu(II) center. However, we note that the intensity of the rising-edge feature might obscure any pre-edge peak. Further insight into the electronic structure of **1** can be obtained by comparing its K-edge position to that of **2**. Visual inspection of the edge energies at half-maximum for **1** and **2** reveals nearly superimposable edges suggesting very similar Cu(II) oxidation states.[47,50] Inspection of the first derivative of the edge (Figure 3A, inset) reveals a slight shift to lower energy for **2** (∼1 eV), but edge shifts between Cu(I) and Cu(II) complexes are typically larger, on the order of 2 eV.[63,64] Finally, we note that the intense shakedown peak in **1** is significantly attenuated and shifted to higher energy in **2**, changes which are consistent with a higher coordination number in **2** versus **1**.[64] In short, the XANES spectra of **1** and **2** are slightly more suggestive of a (DHP$^{2-\bullet}$)Cu(II) electronic structure in **1**, but convolutions prevent a definitive assignment.

To gain more insight into the electronic structure of **1**, particularly regarding the oxidation state at Cu, we undertook computational investigations. Geometries of the singlet and triplet states of the LCu complex were optimized using density functional theory (DFT) at the B3LYP/6-31G* level of theory, revealing a singlet ground state with an adiabatic triplet−singlet gap of $\Delta H(T - S)$ = 3.94 kcal/mol (Figures S40 and S41). To resolve the effects of multireference correlation in a possible (DHP$^{2-\bullet}$)Cu(II) open-shell singlet, further calculations were then carried out using the variational two-electron reduced-density-matrix (V2RDM) complete active space self-

https://doi.org/10.1021/jacs.2c04630
J. Am. Chem. Soc. 2022, 144, 15569−15580

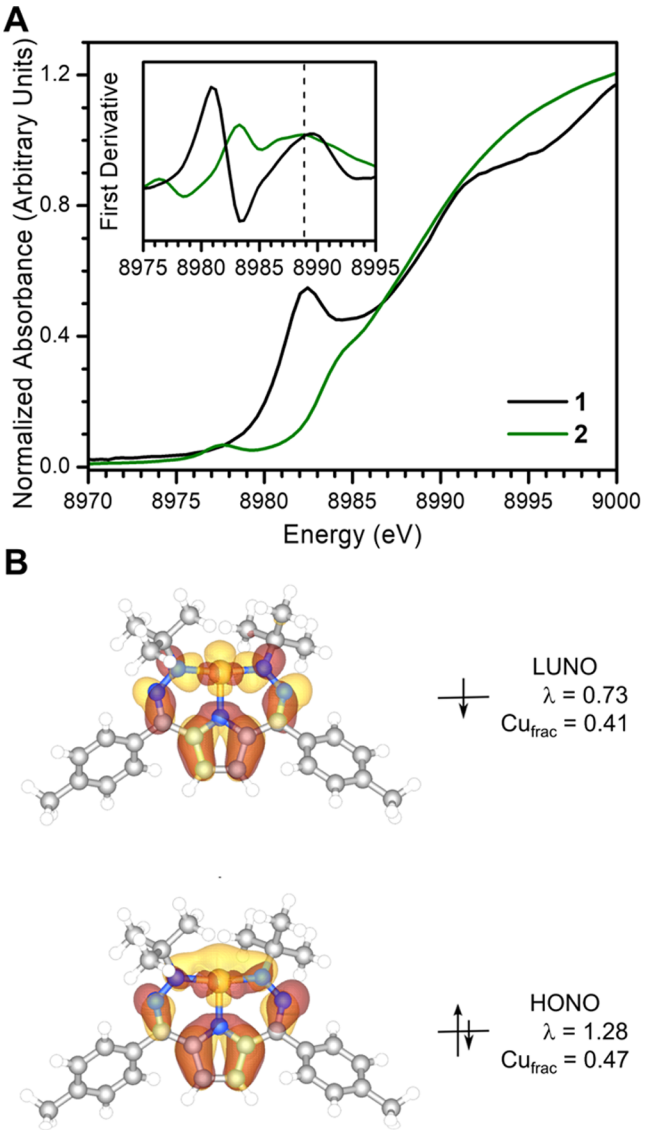

Figure 3. (A) Cu K-edge X-ray absorption data for **1** (black) and **2** (green) with the smoothed first derivative of normalized absorbance (inset). The dashed line indicates the energy at half-maximum normalized absorbance. (B) Frontier natural orbitals and their natural occupation numbers (λ) for **1** along with fractional atomic orbital contributions to the natural orbitals for Cu (Cu_{frac}). Data obtained via [14,14] V2RDM CASSCF calculations with the 6-31G* basis set.

consistent field (CASSCF) method. Utilizing the singlet ground state DFT geometry in combination with an active space of 14 electrons distributed in 14 spatial orbitals, [14,14], and a 6-31G* basis set, the V2RDM calculations also predict a strongly correlated singlet ground state and a vertical triplet−singlet gap of 1.51 kcal/mol.

The singlet ground state displays significant biradical character with frontier natural occupation numbers (NON) of 1.28 and 0.73 for the highest occupied natural orbital (HONO) and the lowest unoccupied natural orbital (LUNO), respectively. A molecular orbital diagram of the frontier natural orbitals shows the unpaired electron density to be delocalized across both the Cu center as well as the π system of the ligand (Figure 3B). To further analyze the delocalization of the unpaired electron density, the fraction of Cu atomic orbital contributions to the frontier NOs was calculated, revealing the HONO and LUNO to be localized to 47 and 41% on the Cu center, respectively (Table S18). Thus, while the bonding in **1** appears to be highly covalent, with contributions from both Cu(I) and Cu(II) limiting resonance structures, the sum of the experimental and theoretical studies suggests that a Cu(II) oxidation state is most appropriate.

Reactivity with O_2. With the assignment of a DHP ligand radical for **1**, we then wanted to determine if this ligand-stored electron could activate O_2 in analogy with proposals for galactose oxidase (GO) and previously observed reactivity with DHP complexes of Ni.[49,50] Addition of an excess of dry O_2 to complex **1** elicits a color change from blue to green and a broadened ^{1}H NMR spectrum indicative of the formation of a paramagnetic product (Scheme 1 and Figure S5). This product has been assigned as an end-on κ^1 Cu−superoxo complex [^{tBu,Tol}DHP$^-$]CuO$_2$ (**3**) based on various spectroscopic methods. The conversion of **1** to **3** was monitored by UV−visible spectroscopy revealing an isosbestic transition (Figure 4A). The intense absorbance of **1** at 618 nm, assigned as a $\pi \rightarrow \pi^*$ transition on the DHP ligand, diminishes as new features centered at 420 and 670 nm arise. The growth of a feature at 420 nm is consistent with an O → Cu charge-transfer absorption frequently observed for Cu−superoxo complexes.[39] The extinction coefficient of the shoulder at 420 nm (13,600 M^{-1} cm^{-1}) is higher than would be expected for an end-on superoxo complex (4,000−5,000 M^{-1} cm^{-1}), but we note overlapping higher-energy absorbances, which likely increase the overall absorbance in this region.[65] The isosbestic transformation occurs at room temperature as well as at −80 °C with no other noticeable intermediates. The rate of the disappearance of the major absorbance of **1** in the presence of excess O_2 can be well-fit to a pseudo-first-order decay (Figure S23).

Raman vibrational spectra were collected on thin films of **3** to confirm the presence of a Cu−superoxo moiety (Figure 4B). Laser excitation at 633 nm gave a band at 1067 cm^{-1} that shifts upon $^{18}O_2$ labeling to 1006 cm^{-1}, consistent with the simple harmonic oscillator predicted shift for an O−O stretch of 60 cm^{-1} and also in good agreement with previous reports of end-on superoxo complexes.[38−40] In contrast, bridging and mononuclear peroxo complexes typically have stretches in the 750−950 cm^{-1} region.[66] We have not identified isotopically sensitive peaks in the Cu−O stretching region; however, these low-energy features are not as easily interpretable, putatively due to coupling to other vibrational modes as suggested by frequency calculations. This data supports the presence of a superoxo ligand in **3**, but we wanted to acquire further data to determine whether the superoxo binding mode was end-on or side-on.

We therefore acquired XAS data on **3** both to understand the electron transfer to form the superoxo as well as to obtain structural characterization on this complex. The XANES region of **3** shows clear changes compared to **1** including a low-intensity pre-edge feature at 8975.5 eV assigned as a 1s → 3d transition (Figure 4C). The intensity of the pre-edge feature depends on the degree of p−d mixing, with DFT calculations predicting the p-orbital contribution to the highest lying d-orbital to be 1.1% (Table S8). The K-edge energies at half-maximum intensity for **1** and **3** are nearly superimposable, consistent with a ligand to an O_2 electron-transfer event as would be expected from the (DHP$^{2-\bullet}$)Cu(II) electronic structure of **1**.[47,50] The extended X-ray absorption fine structure (EXAFS) region was also fit for the first three shells

https://doi.org/10.1021/jacs.2c04630
J. Am. Chem. Soc. 2022, 144, 15569−15580

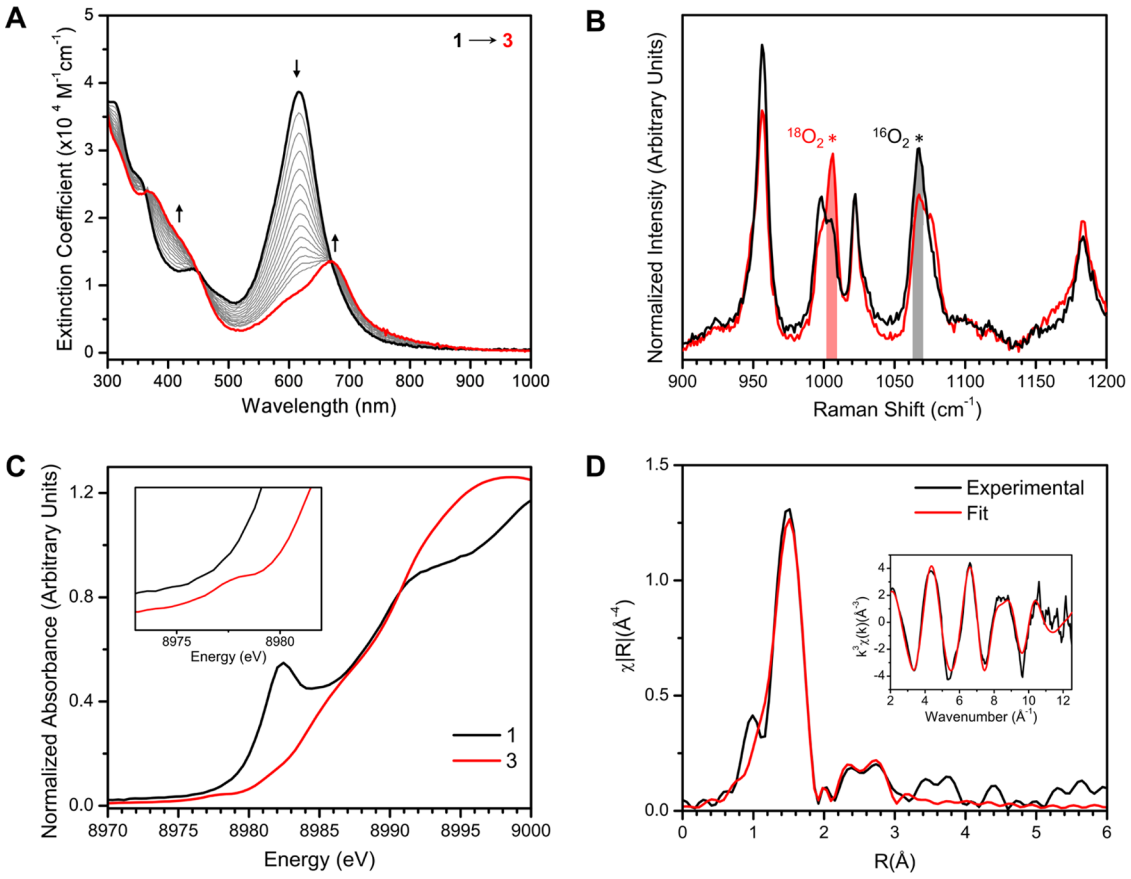

Figure 4. (A) UV−visible spectroscopy of 0.015 mM **1** in DCM at 25 °C upon addition of 2 mL of O_2 where **1** is black and **3** is red. Formation of **3** with scans every 2 min starting 4 min after O_2 addition. The extinction coefficient is based on an initial concentration of **1**, assuming complete conversion to **3**. (B) Variable isotope Raman spectra of the reaction of **1** with O_2 at room temperature to form **3**. The reactions with $^{16}O_2$ versus $^{18}O_2$ are shown in the superoxo stretching region. (C) Cu K-edge X-ray absorption data for **1** (black) and **3** (red) with an expanded pre-edge region (inset). (D) *R*-space EXAFS fitting for **3**, with *k*-space shown in the inset (data, black; fits, red).

surrounding Cu with a *k*-space window from 2 to 12.5 Å^{-1} (Figure 4D). The fit confirms the assignment of an end-on Cu−superoxo complex, with a primary coordination shell (R = 1.94(2) Å) consisting of 4 N/O scatterers (Table S3). The terminal Cu···O scattering path was also fit in the second shell with a distance of R = 2.89(2) Å. This length is in remarkably good agreement with the DFT-computed structure of **3** (see below, Table S4). We note that the inclusion of the superoxo ligand is essential to achieve good fits; removing either the β Cu···O scatterer or the superoxo entirely resulted in worse σ^2 values and larger errors (Table S5).

DFT computations also support the assignment of **3** as an end-on Cu−superoxo complex. The optimized open-shell triplet electronic configuration of **3** is predicted to be 4.6 kcal/mol more stable than the optimized open-shell singlet. Evan's method measurements support the assignment of a triplet ground state with μ_{eff} = 3.1 μ_B (spin only: 2.83 μ_B), although some degradation of the sample convolutes interpretation of this data (Figure S6). The predicted triplet ground state for **3** is unsurprising as there is precedent for triplet states in Cu−superoxo complexes that arise from O−O π^* character mixing with the Cu d_{z^2} orbital.[67] The optimized geometry of **3** has a Cu−O−O angle of 113° and a distance between Cu and the distal O-atom of 2.84 Å, which again matches very well with the parameters obtained from EXAFS fitting (Figure S34).

Oxidative Catalysis and Mechanism. After rigorously characterizing **3** as an open-shell triplet Cu−superoxo complex, we monitored its oxidative reactivity with diphenylhydrazine (DPH) by UV−visible spectroscopy (Figure S24). After monitoring the conversion from **1** to **3** under O_2, the cuvette was purged with N_2 before injecting 10 equiv of DPH. Within 20 s, the main superoxo absorbance at 670 nm was quenched and the characteristic absorbance of **1** at 618 nm along with features from 300 to 450 nm corresponding to azobenzene was observed. This observation supports that **3** is a competent oxidizing species and prompted us to determine whether catalytic oxidations mediated by **3** might be possible (Scheme 2).

Addition of 1 atm of O_2 to either DPH or 1,4-hydroquinone in the presence of 10 mol % of **1** results in the formation of azobenzene and paraquinone, respectively, both in >90% yield (Figures S7 and S10). Catalytic O-atom transfer with triphenylphosphine proceeds similarly with nearly 6 turnovers (Figure S8). This catalytic system is also competent for substrates with homolytically stronger E−H bonds if strong bases are used. Benzyl alcohol conversion to benzaldehyde occurs catalytically if 0.5 equiv of KO^{t}Bu is added to the catalytic mixture (Figure S9). We hypothesize that deprotonation to generate benzyloxide may facilitate alkoxide binding or other subsequent mechanistic steps. We note related deprotonations in the mechanisms of both GO and Cu aminoxyl catalyses, so the need for a base in our system is not

https://doi.org/10.1021/jacs.2c04630
J. Am. Chem. Soc. 2022, 144, 15569−15580

Scheme 2. Catalytic Oxidative Reactivity of 3[a,b]

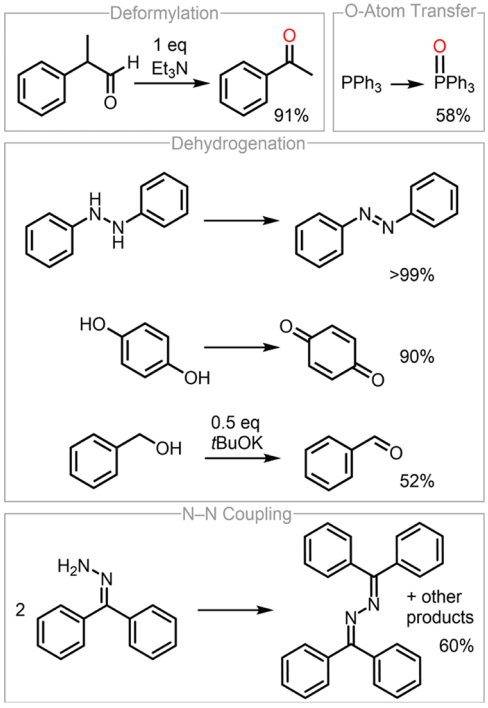

[a]All reactions were carried out with 10 mol % 1 under 1 atm O_2 for 18 h in DCM, with the exception of benzyl alcohol, which was in THF to better tolerate *t*BuOK. [b]Yield is determined by ^{1}H NMR spectroscopy (^{31}P NMR for PPh_3) and is based on integration compared to an internal standard (mesitylene) or the ratio of product/(product + starting material) for PPh_3.

unexpected. The muted reactivity of **1** with other stronger C–H bonds such as dihydroanthracene suggests a weak O–H BDE for the putative Cu–hydroperoxo product. Indeed, DFT calculations predict an O–H BDE of 70 kcal/mol for this species, supporting this hypothesis (Table S7).

Complex **1** also serves as a competent catalyst for oxidative reactivity beyond H-atom abstraction or phosphine oxidation. Catalytic deformylation of 2-phenylpropionaldehyde proceeds with 1 equiv of Et_3N to afford acetophenone in 91% yield (Figure S11). The proposed mechanism for aerobic deformylation involves the initial nucleophilic attack by the superoxo moiety, likely aided in this system by the donating nature of the ^{tBu,Tol}DHP ligand's electron-rich *t*Bu groups.[68] Previously reported examples of aerobic aldehyde deformylation catalysts employ Fe and Co, but this reactivity profile is rare for Cu–superoxo species.[43,45−47]

Inspired by studies of hydrazone oxidation to form diazo compounds by synthetic Cu systems,[69] we also examined the reaction of 10 mol % **1** and benzophenone hydrazone under O_2. This reaction yields a 1:2 mixture of benzophenone and coupled azine with no detectable diazo product (Figure S14). This product mixture has been reported as the result of downstream reactivity of diazo complexes via hydrolysis.[70] While the coupled azine may formally be the product of self-condensation, we note it is not observed in significant quantities from self-decay of the starting hydrazone or in the presence of simple Cu salts as possible Lewis acids (Table S1). This instead suggests an oxidative process, similar to previously reported transformations.[70] Control reactions for all tested catalytic transformations support the importance of the (DHP) Cu complexes in supporting oxidative catalysis. While some examples exhibit background reactivity with simple Cu salts, the (DHP)Cu system shows uniformly higher reactivity (Table S1).

With the catalytic activity of **1** established, we then wanted to understand the mechanism of oxidative catalysis more thoroughly. We first investigated whether O_2 was being reduced directly to water or if H_2O_2 was generated as a byproduct of catalysis. A test for H_2O_2 formation was carried out for the reaction with DPH by the addition of the H_2O_2 selective chemical test agent 1,3-diphenylisobenzofuran (DPBF).[71] Mass spectrometric analysis of the reaction mixture reproducibly showed the formation of the product 9-hydroxyanthracen-10(9*H*)-one, which is diagnostic for the presence of H_2O_2 (Figure S15). Quantification of H_2O_2 via iodometric titration from reactions with hydroquinone shows

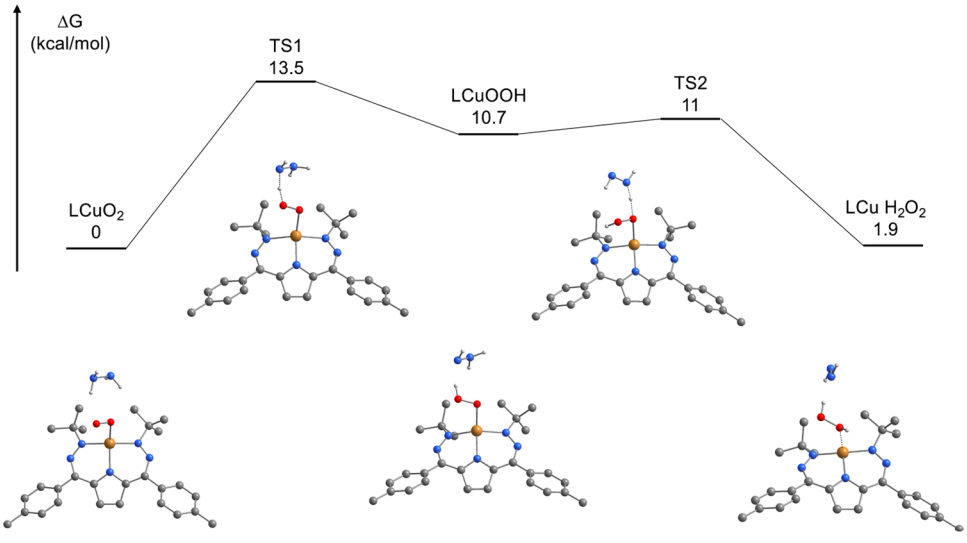

Figure 5. DFT-computed geometries and energies of hydrazine dehydrogenation by **3**. Calculations were carried out with the M06L functional and a def2-TZVP basis set, with a def2-TZVPP basis set for Cu. Cu is shown in orange, C in gray, N in blue, O in red, and H in white. Only H-atoms involved in substrate dehydrogenation are shown.

https://doi.org/10.1021/jacs.2c04630
J. Am. Chem. Soc. 2022, 144, 15569−15580

Scheme 3. Mechanistic Comparison of Synthetic and Biological Cu Aerobic Oxidative Catalysts[a,b]

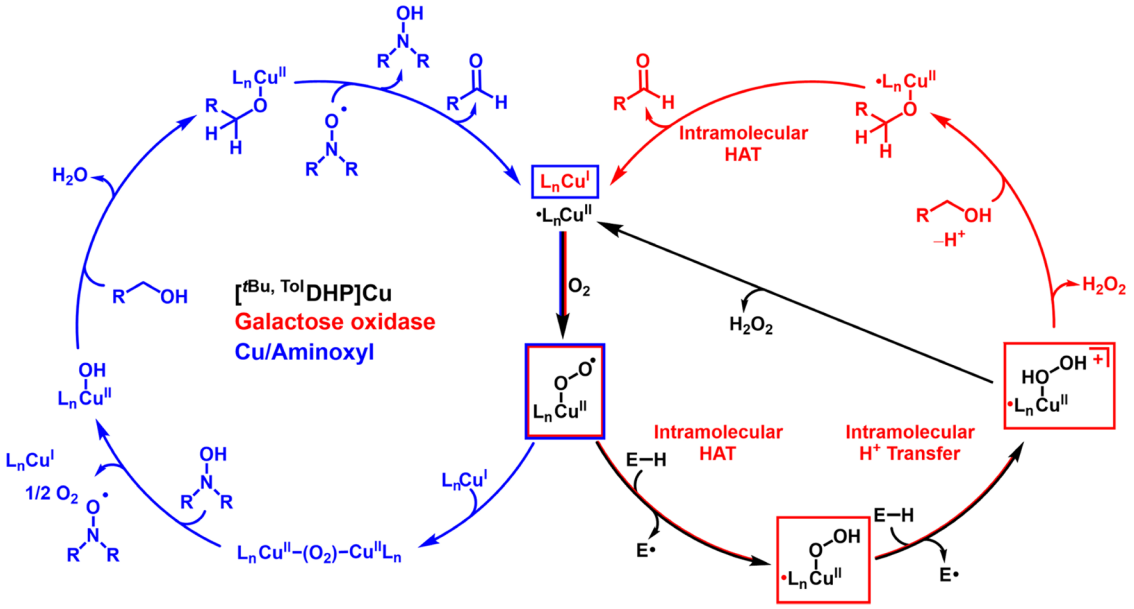

[a]The colored arrows and structures refer to mechanistic steps and intermediates for the [^{t}Bu, ^{Tol}DHP]Cu (black), GO (red), and Cu/aminoxyl (blue) catalytic systems, with overlayed multicolor arrows and boxes notating steps or intermediates that are shared by the indicated systems. [b]Note that the two rightmost steps for GO are intramolecular proton transfers mediated by an active site phenol/phenolate, which is not shown.

that the yield of H_2O_2 is small but reproducible (Table S2 and Figure S18). The formation of H_2O_2 is reasonable for a reaction mechanism where two H-atom equivalents from DPH or hydroquinone are transferred to a superoxo moiety resulting in the azobenzene product and H_2O_2 as a byproduct. The low observed yield of H_2O_2 is consistent with its ability to also serve as an oxidant for either substrates or in situ formed Cu complexes (Figure S27).

The thermodynamic barriers of such a pathway along with putative transition states and intermediates were then investigated using DFT calculations for **3** (Figure 5). Hydrazine was used as a substrate for computational efficiency, assuming that the transition-state barriers should either be similar to or higher than DPH. Calculations comparing the thermodynamic favorability of DPH and hydrazine dehydrogenation predict that the former reaction is approximately 9 kcal/mol more downhill in energy, supporting that the use of hydrazine instead of DPH is a conservative model (Table S14). The first optimized transition state to form a Cu–hydroperoxo intermediate has a barrier of 13.2 kcal/mol, followed by a nearly barrierless (0.3 kcal/mol) second H-atom abstraction. Inspection of the Mulliken charges along the reaction coordinate suggests that each transition state is best described as an H-atom ($H^+ + e^-$) transfer rather than a heterolytic proton and hydride transfer (Table S15). The calculated transition-state barriers are reasonable for a room temperature reaction and show that the Cu–superoxo species is a feasible active oxidant in the dehydrogenation of DPH. These calculations support the hypothesis that **3** is an active oxidant in catalysis. Indeed, we observe substantially enhanced rates of decay of independently generated **3** under N_2 in the presence of substrates (Figure S26).

The muted aerobic catalysis of **1** with alcohol and hydrocarbon substrates prompts questions about the identity of the active oxidant more broadly in aerobic Cu catalysis (Scheme 3). In many Cu/aminoxyl catalytic cycles, the oxidizing species for C–H activation is proposed to be a free or complexed aminoxyl radical.[72,73] In these cases, the primary role of O_2 is proposed to be re-oxidation of the metal center and regeneration of aminoxyl species from hydroxylamines. Parallel trends can be drawn in biological systems. For instance, proposed GO enzymatic cycles involve a H-atom transfer to a coordinating modified tyrosyl radical residue along with electron transfer to the Cu center as the active alcohol oxidizing steps, with O_2 serving to regenerate the oxidized active site.[74] Conversely, studies of lytic polysaccharide monooxygenase (LPMO) active sites implicate a more direct substrate oxidizing role for O_2-derived species such as Cu oxyl or Cu hydroxo species.[75,76] While several Cu–superoxo complexes have been shown to initiate the oxidation of moderately strong C–H and O–H bonds (BDEs of ~70–83 k cal^{-1} mol^{-1}), most model systems have not been able to mimic the reactivity of monooxygenase enzymes, which commonly activate C–H bonds with strengths of up to 87 k cal^{-1} mol^{-1}.[77−80]

We observe no hydroxylation reactivity with aliphatic C–H substrates in the present system. This observation supports the proposed mechanistic paradigms of synthetic Cu systems and GO where oxygenated Cu species are primarily invoked as intermediates en route to the active oxidizing species as opposed to directly oxidizing substrates. In this way, the importance of metal–ligand cooperativity in these systems is further underscored in that the supporting ligand (or co-catalyst in the case of aminoxyl systems) must be suitably oxidizing to directly react with substrates to be regenerated by, or otherwise react with, O_2. Indeed, while we observe that DPH is readily converted to azobenzene by the oxidized (DHP^-) complex **2**, this complex shows no reactivity with other substrates such as alcohols or hydrocarbons under N_2 (Table S1). Conversely, the oxidative deformylation and phosphine oxidation reactivity must stem from an oxygenated Cu compound, i.e., **3**. Thus, our studies suggest that while

https://doi.org/10.1021/jacs.2c04630
J. Am. Chem. Soc. 2022, 144, 15569−15580

Cu−superoxo complexes are important catalytic species in aerobic oxidative reactivity, for instance in reactions with net O-atom transfer or in the activation of weak E−H bonds, in more demanding dehydrogenation cycles, they may be more commonly involved in regenerating the active species as opposed to directly oxidizing substrates themselves.

CONCLUSIONS

Herein, we have described the synthesis and characterization of a mononuclear Cu complex with a T-shaped geometry. Detailed spectroscopic and computational investigations support a ligand-radical Cu(II) electronic structure for this complex. Addition of O_2 at room temperature results in the formation of a superoxo complex, which has been thoroughly characterized by several spectroscopic methods. This complex is a catalyst at room temperature for the aerobic oxidation of hydrazine, alcohol, phosphine, aldehyde, and hydrazone substrates.

This work represents an unusual example of a thoroughly characterized Cu−superoxo complex, which also mediates aerobic oxidation. The predicted weak BDE of a putative Cu−hydroperoxo intermediate and the observed sluggish reactivity of this system toward alcohols and hydrocarbons suggest that superoxo intermediates may commonly feature in the regeneration of active substrate oxidants in aerobic catalysis as opposed to featuring as active oxidants themselves. This proposal underscores the importance of metal−ligand cooperativity in aerobic catalysis in the design of synthetic systems.

EXPERIMENTAL SECTION

General Considerations. All reagents were purchased from commercial suppliers and used without further purification unless otherwise specified. All manipulations were carried out under an atmosphere of N_2 using standard Schlenk and glovebox techniques. Glassware was dried at 180 °C for a minimum of 2 h and cooled under vacuum prior to use. Solvents were dried on a solvent purification system from Pure Process Technology, passed over a column of activated alumina, and stored over 4 Å molecular sieves under N_2. Tetrahydrofuran was stirred over NaK alloy and run through an additional activated alumina column prior to use to ensure dryness. C_6D_6, CD_2Cl_2, and d_8-THF were stored over 4 Å molecular sieves under N_2. Solvents were tested for H_2O and O_2 using a standard solution of the sodium-benzophenone ketyl radical anion. O_2 was passed through a packed Drierite (calcium sulfate, anhydrous) drying agent before addition to the reaction vessel.

^{1}H, ^{31}P{^{1}H}, and ^{19}F{^{1}H} NMR spectra were recorded on a Bruker DRX 400 or 500 MHz spectrometer. Chemical shifts are reported in ppm units referenced to residual solvent resonances for ^{1}H spectra, UV−visible spectra were recorded on a Thermo Evolution 300 spectrometer, and the addition of gases was performed by injecting via a syringe into a cuvette sealed with a septum. UV−visible spectra at low temperature were recorded using a Unisoku cryostat. Raman spectra were recorded using a Horiba LabRAM HR Evolution system. EPR spectra were recorded on an Elexsys E500 spectrometer with an Oxford ESR 900 X-band cryostat and a Bruker Cold-Edge Stinger and were simulated using the Easyspin suite in Matlab software.[81] Gas chromatography/mass spectrometry (GC/MS) was collected on an Agilent SQ GC/MS with 5977A single quad MS and 7890B GC. Elemental analysis was performed by Midwest Microlabs. Electrochemical measurements were performed using a BAS Epsilon potentiostat and analyzed using BAS Epsilon software version 1.40.67NT. Cyclic voltammetry measurements were made using a glassy carbon working electrode, platinum wire counter electrode, and silver wire pseudo-reference electrode and were referenced to internal Fc/Fc^+.

X-ray Structure Determination. The diffraction data were measured at 100 K on a Bruker D8 VENTURE with a PHOTON 100 CMOS detector system equipped with a Mo-target microfocus X-ray tube (λ = 0.71073 Å). Data reduction and integration were performed with the Bruker APEX3 software package (Bruker AXS, version 2015.5-2, 2015). Data were scaled and corrected for absorption effects using the multiscan procedure implemented in SADABS (Bruker AXS, version 2014/5, 2015, part of the Bruker APEX3 software package and APEX4 software package). The structure was solved by the dual method implemented in SHELXT and refined by a full-matrix least-squares procedure using the OLEX2 software package (XL refinement program version 2014/7). Suitable crystals were mounted on a cryo-loop and transferred into the cold nitrogen stream of the Bruker D8 Venture diffractometer. Most of the hydrogen atoms were generated by geometrical considerations, constrained to idealized geometries, and allowed to ride on their carrier atoms with an isotropic displacement parameter related to the equivalent displacement parameter of their carrier atoms. Compound **1** was modeled for the three-component disorder of one of the *p*-Tol rings. For compound **2**, a solvent mask as implemented in OLEX2 was used as the exact solvent composition could not be identified. A mixture of solvents was used for crystallization and the presence of multiple solvents was identified by NMR.

X-ray Absorption Measurements. Frozen solution samples were prepared by making a 0.02 M solution of **1** in THF of the starting material for **1** and **2**, and for **3**, the solution was removed from the glovebox and reacted with O_2 by syringing the gas into the sample and bubbling through. For sample solutions of **1**, **2**, and **3**, the solution was transferred with a syringe to a Teflon window lined with Kapton tape. The solution was frozen using liquid nitrogen and then stored in liquid nitrogen until collection. Data were acquired at the Advanced Photon Source at the Argonne National Laboratory with a bending magnet source with ring energy at 7.00 GeV. Cu K-edge data were acquired at the MRCAT 10-BM beam line. The incident, transmitted, and reference X-ray intensities were monitored using gas ionization chambers. A metallic Cu foil standard was used as a reference for energy calibration and was measured simultaneously with experimental samples. X-ray absorption spectra were collected at room temperature. The first inflection point of the foil spectrum was assigned to 8978.9 eV. Normalization and background subtraction of the data were performed using Athena from the Demeter software suite. The EXAFS curve-fitting analysis program OPT in EXAFSPAK (George, G.N. Stanford Synchrotron Radiation Laboratory: Stanford, CA, 2000) was used to fit the EXAFS data. The theoretical paths were generated using FEFF (version 7.0). The starting structural model for **3** was obtained from the DFT optimized structure. During the fitting process, the bond distance (R) and the mean-square thermal and static deviation in R (σ^2) were allowed to vary. The threshold energy (E_0) was allowed to vary but was constrained as a common value for all components in a given fit. The amplitude reduction factor (S_0^2) was fixed at 0.9 and the coordination numbers (N) were systematically varied to achieve the best fit.

Synthesis of [^{tBu,Tol}DHP•]Cu (1). To a stirring THF (10 mL) solution of ^{tBu,Tol}DHP·2 HCl (100 mg, 0.19 mmol) was added 2.5 M *n*-BuLi in hexanes (0.31 mL, 4 equiv), which turned the solution from yellow to red. The red mixture was stirred for 5 min before adding 1-hexene (12 μL, 0.5 equiv), and the resulting mixture was added to a stirring slurry of $CuCl_2$ in THF (27 mg, 0.19 mmol, 1 equiv), turning deep blue. 1-Hexene is thought to serve as an H-atom acceptor and improves the yield of the metalation moderately. After stirring for 2 h, the solution was filtered and all volatiles were removed under vacuum, resulting in a dark blue residue. The residue was taken up in benzene, passed through a silica plug, and then evaporated under vacuum to give **1** as a blue powder. Yield: 47 mg, 0.09 mmol, 37%. Single crystals suitable for X-ray diffraction were obtained by crystallization from concentrated petroleum ether at −35 °C. ^{1}H NMR (400 MHz, C_6D_6, 25 °C): δ 7.87 (d, 4H), 7.67 (s, 2H), 7.19 (d, 4H), 2.24 (s, 6H), 1.69 (s, 18H). ^{13}C{^{1}H} NMR (125 MHz, C_6D_6, 25 °C) δ 142.02, 138.75, 137.02, 135.59, 134.03, 131.38, 129.39, 69.62, 30.81, 21.22. UV−visible spectrum (DCM solution): 440 nm (ε_0 12,400 $M^{-1}cm^{-1}$), 616

https://doi.org/10.1021/jacs.2c04630
J. Am. Chem. Soc. 2022, 144, 15569−15580

nm (ε_0 38,700 $M^{-1}cm^{-1}$).IR (nujol mull, cm^{-1}): 2720 (m), 2672 (m), 1510 (s, C═N), 1297 (s), 1254 (m), 1171 (s), 1091 (m), 1016 (m), 823 (s), 785 (m), 720 (s). Anal. Calc. C, 66.7; H, 6.8; N, 13.9; Found: C, 66.9; H, 7.1; N, 13.0. HRA-MS (m/z) $[M]^+$ $C_{28}H_{34}CuN_5$: 503.211 Found: 503.211. Bulk purity was also determined to be 99.5% by ^1H NMR referenced to a mesitylene internal standard (Figure S12).

*Synthesis of [^{tBu,Tol}DHP]CuOTf (**2**).* To a stirring solution of **1** in THF (0.020 g, 0.04 mmol, 5 mL) was added a THF (2 mL) solution of AgOTf (0.01 g, 2 mL, 1 equiv), resulting in a color change from blue to deep green. The reaction was stirred for 30 min, filtered, and evaporated under vacuum. Single crystals suitable for X-ray diffraction were obtained from a concentrated petroleum ether solution at −35 °C. ^1H NMR (400 MHz, C_6D_6, 25 °C): 7.54, 5.93, 3.86, 2.04, 1.34. $^{19}F\{^1H\}$ NMR (125 MHz, C_6D_6, 25 °C) δ −74.08. Evans method (C_6D_6, 25 °C, μ_B) μ_{eff} = 1.72. UV−visible spectrum (DCM solution): 448 nm (ε_0 11,200 M^{-1} cm^{-1}), 638 nm (ε_0 11,300 M^{-1} cm^{-1}), 704 nm (shoulder). IR (nujol mull, cm^{-1}): 2720 (m), 2667 (m), 1306 (m), 1267 (m), 1167 (s), 1101 (m), 1006 (s), 960 (m), 887 (m), 843 (m). Anal. Calc. C, 53.3; H, 5.3; N, 10.7; Found: C, 53.2; H, 5.0; N, 10.5. HRA-MS (m/z) $[M]^+$ $C_{29}H_{34}CuF_3N_5O_3S$: 652.163 Found: 652.173.

*Synthesis of [^{tBu,Tol}DHP]CuO$_2$ (**3**).* A solution of **1** in DCM (or THF) was removed from the glovebox, and an excess of dry O_2 was bubbled through the solution using a 500 μL gas syringe, resulting in a color change from blue to green. The completeness of the reaction was tracked by taking aliquots for UV−visible spectroscopy. UV−visible spectrum (DCM solution): 420 nm (ε_0 16,900 M^{-1} cm^{-1}) and 670 nm (ε_0 13,600 M^{-1} cm^{-1}).

*Raman Sample Preparation of **3**.* A concentrated solution of **1** in DCM was removed from the glovebox in a sealed vial with a septum. O_2 was syringed into the vial (3 mL), and the reaction was allowed to stir as the solution turned green, indicating formation of **3**. The reaction progress could be tracked by diluting aliquots and taking a UV−vis spectrum. When the conversion to **3** was complete, the concentrated solution was drop-cast onto a glass microscope slide under a positive flow of N_2 that rapidly evaporated the solvent. The sample was then covered with a microscope cover glass, and an adhesive spacer sealed the sample between the microscope slide and cover glass to prevent contact with air during data collection. The Raman spectrum was collected with a 633 nm laser on 1% power, 30 s acquisition times, 12 acquisitions, and a 50× LWD microscope objective.

Oxidative Reactivity. In a nitrogen glovebox, to a solution of **1** in CD_2Cl_2 (1 mg, 0.002 mmol) were added diphenylhydrazine (4 mg, 0.02 mmol, 10 equiv) and mesitylene (2.8 μL). This was added to a 50 mL Schlenk tube with a stir bar and removed from the box. After one freeze pump thaw cycle, the tube was charged with 1 atm of dry O_2 and stirred overnight. The solution was then transferred to an NMR tube for product characterization. For benzyl alcohol, ^{t}BuOK (1 mg, 0.01 mmol, 5 equiv) was added along with the substrate. For 2-phenylpropionaldehyde, Et_3N (2.8 μL, 0.02 mmol, 10 equiv) was added to the substrate. ^1H NMR yields were determined by integration against the internal mesitylene standard. $^{31}P\{^1H\}$ NMR yields for the oxidation of PPh_3 were determined from the ratio of product/(product + starting material) integrations. Yields for benzophenone hydrazone oxidation were determined by gas chromatography (versus a mesitylene internal standard) due to overlapping NMR signals for the different product species and the starting material.

Reactivity with Diphenylisobenzofuran (DPBF). In a 100 mL Schlenk tube, **1** (1 mg, 0.002 mmol), diphenylhydrazine (DPH) (4 mg, 0.02 mmol), and DPBF (5 mg, 0.02 mmol) were dissolved in DCM (0.5 mL). After 1 freeze pump thaw cycle, the tube was charged with 1 atm O_2 and allowed to react for 1 h (this completion time with DPH was previously determined by ^1H NMR). The product mixture was then diluted with DCM to 1.5 mL, filtered, and analyzed by GC/MS.

Computational Methodology. For V2RDM CASSCF, geometry optimizations were carried out with DFT, utilizing the B3LYP functional[82] in combination with the 6-31G* basis set,[83] as implemented in Gaussian 16 Rev. A.03.[84] Multireference correlation was resolved with variational two-electron reduced-density-matrix (V2RDM) complete active space self-consistent field (CASSCF)[85,86] calculations as implemented in the Maple Quantum Chemistry Package.[87,88] V2RDM calculations utilized an active space of 14 electrons distributed in 14 spatial orbitals, [14,14], and a 6-31G* basis set. Structures of **3** as well as the intermediates and transition states for the reaction coordinate with hydrazine were optimized in ORCA[89] using the M06L functional and def2-TZVPP basis set on Cu, def2-TZVP basis set on all other atoms. Frequency calculations were performed to confirm the structures are at local minima on the potential energy surface.

■ ASSOCIATED CONTENT

Supporting Information

The Supporting Information is available free of charge at https://pubs.acs.org/doi/10.1021/jacs.2c04630.

Experimental procedures, NMR, GC/MS, UV−visible, EPR, XAS, electrochemistry, SXRD data, and DFT (PDF)

Accession Codes

CCDC 2168980−2168981 contain the supplementary crystallographic data for this paper. These data can be obtained free of charge via www.ccdc.cam.ac.uk/data_request/cif, or by emailing data_request@ccdc.cam.ac.uk, or by contacting The Cambridge Crystallographic Data Centre, 12 Union Road, Cambridge CB2 1EZ, UK; fax: +44 1223 336033.

X-ray crystallographic data for 1 and 2 (CIF)

■ AUTHOR INFORMATION

Corresponding Author

John S. Anderson − *Department of Chemistry, University of Chicago, Chicago, Illinois 60637, United States;* orcid.org/0000-0002-0730-3018; Email: jsanderson@uchicago.edu

Authors

Maia E. Czaikowski − *Department of Chemistry, University of Chicago, Chicago, Illinois 60637, United States;* orcid.org/0000-0002-1334-8140

Andrew J. McNeece − *Department of Chemistry, University of Chicago, Chicago, Illinois 60637, United States;* Present Address: Los Alamos National Laboratory, Los Alamos, New Mexico 87545, United States; orcid.org/0000-0001-8381-6539

Jan-Niklas Boyn − *Department of Chemistry, University of Chicago, Chicago, Illinois 60637, United States;* orcid.org/0000-0002-6240-3759

Kate A. Jesse − *Department of Chemistry, University of Chicago, Chicago, Illinois 60637, United States;* Present Address: Los Alamos National Laboratory, Los Alamos, New Mexico 87545, United States; orcid.org/0000-0002-3527-4007

Sophie W. Anferov − *Department of Chemistry, University of Chicago, Chicago, Illinois 60637, United States;* orcid.org/0000-0003-3972-5845

Alexander S. Filatov − *Department of Chemistry, University of Chicago, Chicago, Illinois 60637, United States;* orcid.org/0000-0002-8378-1994

David A. Mazziotti − *Department of Chemistry, University of Chicago, Chicago, Illinois 60637, United States;* orcid.org/0000-0002-9938-3886

Complete contact information is available at:
https://pubs.acs.org/10.1021/jacs.2c04630

Notes

The authors declare no competing financial interest.

■ ACKNOWLEDGMENTS

This work was supported by the National Institutes of Health (R35 GM133470) and as part of the Inorganometallic Catalysis Design Center, an Energy Frontier Research Center funded by the Department of Energy, Office of Science, Basic Energy Sciences (DE-SC0012702). The authors thank the University of Chicago for funding and the Sloan Foundation for a Research Fellowship to J.S.A. (FG-2019-11497). The authors thank Joseph Schneider for assistance with EPR measurements, and they thank Norman Zhao and Jorge Martinez for assistance with XAS measurements. They also thank the Research Computing Cluster at the University of Chicago for providing computing resources. This work made use of the shared facilities at the University of Chicago Materials Research Science and Engineering Center, supported by the National Science Foundation under award number DMR-2011854. MRCAT operations are supported by the Department of Energy and the MRCAT member institutions. This research used resources of the Advanced Photon Source, a Department of Energy (DOE) Office of Science User Facility operated for the DOE Office of Science by Argonne National Laboratory under Contract No. DE-AC02-06CH11357. The authors thank Dr. Joshua Wright and Dr. Yujia Ding for their assistance at 10-BM.

■ REFERENCES

(1) Arends, I. W. C. E.; Sheldon, R. A.; Bäckwall, J. E. Modern Oxidation of Alcohols Using Environmentally Benign Oxidants. *Mod. Oxid. Methods*, Wiley-VCH, 2010, 147−185.
(2) Caron, S.; Dugger, R. W.; Ruggeri, S. G.; Ragan, J. A.; Ripin, D. H. B. Large-Scale Oxidations in the Pharmaceutical Industry. *Chem. Rev.* **2006**, *106*, 2943−2989.
(3) Piancatelli, G.; Scettri, A.; D'auria, M. Pyridinium chlorochromate: a versatile oxidant in organic synthesis. *Synthesis* **1982**, *1982*, 245−258.
(4) Corey, E. J.; Suggs, J. W. Pyridinium chlorochromate. An efficient reagent for oxidation of primary and secondary alcohols to carbonyl compounds. *Tetrahedron Lett.* **1975**, *16*, 2647−2650.
(5) Taylor, R. J. K.; Reid, M.; Foot, J.; Raw, S. A. Tandem Oxidation Processes Using Manganese Dioxide: Discovery, Applications, and Current Studies. *Acc. Chem. Res.* **2005**, *38*, 851−869.
(6) Chandra, P.; Ghosh, T.; Choudhary, N.; Mohammad, A.; Mobin, S. M. Recent advancement in oxidation or acceptorless dehydrogenation of alcohols to valorised products using manganese based catalysts. *Coord. Chem. Rev.* **2020**, *411*, No. 213241.
(7) Cella, J. A.; Kelley, J. A.; Kenehan, E. F. Nitroxide-catalyzed oxidation of alcohols using m-chloroperbenzoic acid. New method. *J. Org. Chem.* **1975**, *40*, 1860−1862.
(8) Kim, H. R.; Jung, J. H.; Kim, J. N.; Ryu, E. K. Oxidation of Benzylic and Secondary Alcohols Using m-Chloroperbenzoic Acid/Hydrogen Chloride/N,N-Dimethylformamide System. *Synth. Commun.* **1990**, *20*, 637−640.
(9) De Mico, A.; Margarita, R.; Parlanti, L.; Vescovi, A.; Piancatelli, G. A Versatile and Highly Selective Hypervalent Iodine (III)/2,2,6,6-Tetramethyl-1-piperidinyloxyl-Mediated Oxidation of Alcohols to Carbonyl Compounds. *J. Org. Chem.* **1997**, *62*, 6974−6977.
(10) Yoshimura, A.; Zhdankin, V. V. Advances in Synthetic Applications of Hypervalent Iodine Compounds. *Chem. Rev.* **2016**, *116*, 3328−3435.
(11) Maity, A.; Hyun, S.-M.; Powers, D. C. Oxidase catalysis via aerobically generated hypervalent iodine intermediates. *Nat. Chem.* **2018**, *10*, 200−204.
(12) Semmelhack, M. F.; Schmid, C. R.; Cortes, D. A.; Chou, C. S. Oxidation of alcohols to aldehydes with oxygen and cupric ion, mediated by nitrosonium ion. *J. Am. Chem. Soc.* **1984**, *106*, 3374−3376.
(13) Hoover, J. M.; Stahl, S. S. Highly Practical Copper(I)/TEMPO Catalyst System for Chemoselective Aerobic Oxidation of Primary Alcohols. *J. Am. Chem. Soc.* **2011**, *133*, 16901−16910.
(14) Markó, I. E.; Giles, P. R.; Tsukazaki, M.; Chellé-Regnaut, I.; Gautier, A.; Brown, S. M.; Urch, C. J. Efficient, Ecologically Benign, Aerobic Oxidation of Alcohols. *J. Org. Chem.* **1999**, *64*, 2433−2439.
(15) Dijksman, A.; Arends, I. W. C. E.; Sheldon, R. A. Cu(ii)-nitroxyl radicals as catalytic galactose oxidase mimics. *Org. Biomol. Chem.* **2003**, *1*, 3232−3237.
(16) Asami, K.; Takashina, A.; Kobayashi, M.; Iwatsuki, S.; Yajima, T.; Kochem, A.; van Gastel, M.; Tani, F.; Kohzuma, T.; Thomas, F.; Shimazaki, Y. Characterization of one-electron oxidized copper(ii)-salophen-type complexes; effects of electronic and geometrical structures on reactivities. *Dalton Trans.* **2014**, *43*, 2283−2293.
(17) Chaudhuri, P.; Hess, M.; Weyhermüller, T.; Wieghardt, K. Aerobic Oxidation of Primary Alcohols by a New Mononuclear CuII-Radical Catalyst. *Angew. Chem., Int. Ed.* **1999**, *38*, 1095−1098.
(18) Chaudhuri, P.; Hess, M.; Müller, J.; Hildenbrand, K.; Bill, E.; Weyhermüller, T.; Wieghardt, K. Aerobic Oxidation of Primary Alcohols (Including Methanol) by Copper(II)− and Zinc(II)−Phenoxyl Radical Catalysts. *J. Am. Chem. Soc.* **1999**, *121*, 9599−9610.
(19) Rajabimoghadam, K.; Darwish, Y.; Bashir, U.; Pitman, D.; Eichelberger, S.; Siegler, M. A.; Swart, M.; Garcia-Bosch, I. Catalytic Aerobic Oxidation of Alcohols by Copper Complexes Bearing Redox-Active Ligands with Tunable H-Bonding Groups. *J. Am. Chem. Soc.* **2018**, *140*, 16625−16634.
(20) Iovan, D. A.; Wrobel, A. T.; McClelland, A. A.; Scharf, A. B.; Edouard, G. A.; Betley, T. A. Reactivity of a stable copper−dioxygen complex. *Chem. Commun.* **2017**, *53*, 10306−10309.
(21) Neira, A. C.; Martínez-Alanis, P. R.; Aullón, G.; Flores-Alamo, M.; Zerón, P.; Company, A.; Chen, J.; Kasper, J. B.; Browne, W. R.; Nordlander, E.; Castillo, I. Oxidative Cleavage of Cellobiose by Lytic Polysaccharide Monooxygenase (LPMO)-Inspired Copper Complexes. *ACS Omega* **2019**, *4*, 10729−10740.
(22) Bhadra, M.; Transue, W. J.; Lim, H.; Cowley, R. E.; Lee, J. Y. C.; Siegler, M. A.; Josephs, P.; Henkel, G.; Lerch, M.; Schindler, S.; Neuba, A.; Hodgson, K. O.; Hedman, B.; Solomon, E. I.; Karlin, K. D.; Thioether-Ligated, A. Cupric Superoxide Model with Hydrogen Atom Abstraction Reactivity. *J. Am. Chem. Soc.* **2021**, *143*, 3707−3713.
(23) Sánchez-Eguía, B. N.; Flores-Alamo, M.; Orio, M.; Castillo, I. Side-on cupric−superoxo triplet complexes as competent agents for H-abstraction relevant to the active site of PHM. *Chem. Commun.* **2015**, *51*, 11134−11137.
(24) Kunishita, A.; Kubo, M.; Sugimoto, H.; Ogura, T.; Sato, K.; Takui, T.; Itoh, S. Mononuclear Copper(II)−Superoxo Complexes that Mimic the Structure and Reactivity of the Active Centers of PHM and DβM. *J. Am. Chem. Soc.* **2009**, *131*, 2788−2789.
(25) Bhat, I. A.; Avinash, I.; Sachan, S. K.; Singh, S.; Anantharaman, G. Efficient Synthesis of Cu(II)-N-Heterocyclic Carbene Complexes in Water and Their Activity Towards Aerobic Alcohol Oxidation. *Eur. J. Inorg. Chem.* **2021**, *2021*, 4560−4565.
(26) Betzemeier, B.; Cavazzini, M.; Quici, S.; Knochel, P. Copper-catalyzed aerobic oxidation of alcohols under fluorous biphasic conditions. *Tetrahedron Lett.* **2000**, *41*, 4343−4346.
(27) Kirillova, M. V.; Fernandes, T. A.; André, V.; Kirillov, A. M. Mild C−H functionalization of alkanes catalyzed by bioinspired copper(ii) cores. *Org. Biomol. Chem.* **2019**, *17*, 7706−7714.
(28) Boldron, C.; Özalp-Yaman, Ş.; Gamez, P.; Tooke, D. M.; Spek, A. L.; Reedijk, J. Selective copper(ii)-mediated oxidative coupling of a nucleophilic reagent to the para-methyl group of 2,4,6-trimethylphenol. *Dalton Trans.* **2005**, *21*, 3535−3541.

(29) Bolm, C.; Schlingloff, G.; Bienewald, F. Copper- and vanadium-catalyzed asymmetric oxidations. *J. Mol. Catal. A: Chem.* **1997**, *117*, 347−350.
(30) Zultanski, S. L.; Zhao, J.; Stahl, S. S. Practical Synthesis of Amides via Copper/ABNO-Catalyzed Aerobic Oxidative Coupling of Alcohols and Amines. *J. Am. Chem. Soc.* **2016**, *138*, 6416−6419.
(31) Bower, J. K.; Cypcar, A. D.; Henriquez, B.; Stieber, S. C. E.; Zhang, S. C(sp3)−H Fluorination with a Copper(II)/(III) Redox Couple. *J. Am. Chem. Soc.* **2020**, *142*, 8514−8521.
(32) Que, L.; Tolman, W. B. Biologically inspired oxidation catalysis. *Nature* **2008**, *455*, 333−334.
(33) Walton, P. H.; Davies, G. J. On the catalytic mechanisms of lytic polysaccharide monooxygenases. *Curr. Opin. Chem. Biol.* **2016**, *31*, 195−207.
(34) Kjaergaard, C. H.; Qayyum, M. F.; Wong, S. D.; Xu, F.; Hemsworth, G. R.; Walton, D. J.; Young, N. A.; Davies, G. J.; Walton, P. H.; Johansen, K. S.; Hodgson, K. O.; Hedman, B.; Solomon, E. I. Spectroscopic and computational insight into the activation of O_2 by the mononuclear Cu center in polysaccharide monooxygenases. *Proc. Natl. Acad. Sci. U.S.A.* **2014**, *111*, 8797−8802.
(35) Lee, J. Y.; Peterson, R. L.; Ohkubo, K.; Garcia-Bosch, I.; Himes, R. A.; Woertink, J.; Moore, C. D.; Solomon, E. I.; Fukuzumi, S.; Karlin, K. D. Mechanistic Insights into the Oxidation of Substituted Phenols via Hydrogen Atom Abstraction by a Cupric−Superoxo Complex. *J. Am. Chem. Soc.* **2014**, *136*, 9925−9937.
(36) Würtele, C.; Gaoutchenova, E.; Harms, K.; Holthausen, M. C.; Sundermeyer, J.; Schindler, S. Crystallographic Characterization of a Synthetic 1:1 End-On Copper Dioxygen Adduct Complex. *Angew. Chem., Int. Ed.* **2006**, *45*, 3867−3869.
(37) Komiyama, K.; Furutachi, H.; Nagatomo, S.; Hashimoto, A.; Hayashi, H.; Fujinami, S.; Suzuki, M.; Kitagawa, T. Dioxygen Reactivity of Copper(I) Complexes with Tetradentate Tripodal Ligands Having Aliphatic Nitrogen Donors: Synthesis, Structures, and Properties of Peroxo and Superoxo Complexes. *Bull. Chem. Soc. Jap.* **2004**, *77*, 59−72.
(38) Donoghue, P. J.; Gupta, A. K.; Boyce, D. W.; Cramer, C. J.; Tolman, W. B. An Anionic, Tetragonal Copper(II) Superoxide Complex. *J. Am. Chem. Soc.* **2010**, *132*, 15869−15871.
(39) Weitzer, M.; Schindler, S.; Brehm, G.; Schneider, S.; Hörmann, E.; Jung, B.; Kaderli, S.; Zuberbühler, A. D. Reversible Binding of Dioxygen by the Copper(I) Complex with Tris(2-dimethylaminoethyl)amine (Me6tren) Ligand. *Inorg. Chem.* **2003**, *42*, 1800−1806.
(40) Maiti, D.; Fry, H. C.; Woertink, J. S.; Vance, M. A.; Solomon, E. I.; Karlin, K. D. A 1:1 Copper−Dioxygen Adduct is an End-on Bound Superoxo Copper(II) Complex which Undergoes Oxygenation Reactions with Phenols. *J. Am. Chem. Soc.* **2007**, *129*, 264−265.
(41) Bhadra, M.; Lee, J. Y. C.; Cowley, R. E.; Kim, S.; Siegler, M. A.; Solomon, E. I.; Karlin, K. D. Intramolecular Hydrogen Bonding Enhances Stability and Reactivity of Mononuclear Cupric Superoxide Complexes. *J. Am. Chem. Soc.* **2018**, *140*, 9042−9045.
(42) Woertink, J. S.; Tian, L.; Maiti, D.; Lucas, H. R.; Himes, R. A.; Karlin, K. D.; Neese, F.; Würtele, C.; Holthausen, M. C.; Bill, E.; Sundermeyer, J.; Schindler, S.; Solomon, E. I. Spectroscopic and Computational Studies of an End-on Bound Superoxo-Cu(II) Complex: Geometric and Electronic Factors That Determine the Ground State. *Inorg. Chem.* **2010**, *49*, 9450−9459.
(43) Abe, T.; Hori, Y.; Shiota, Y.; Ohta, T.; Morimoto, Y.; Sugimoto, H.; Ogura, T.; Yoshizawa, K.; Itoh, S. Cupric-superoxide complex that induces a catalytic aldol reaction-type C−C bond formation. *Commun. Chem.* **2019**, *2*, No. 12.
(44) Concia, A. L.; Beccia, M. R.; Orio, M.; Ferre, F. T.; Scarpellini, M.; Biaso, F.; Guigliarelli, B.; Réglier, M.; Simaan, A. J. Copper Complexes as Bioinspired Models for Lytic Polysaccharide Monooxygenases. *Inorg. Chem.* **2017**, *56*, 1023−1026.
(45) Winslow, C.; Lee, H. B.; Field, M. J.; Teat, S. J.; Rittle, J. Structure and Reactivity of a High-Spin, Nonheme Iron(III)-Superoxo Complex Supported by Phosphinimide Ligands. *J. Am. Chem. Soc.* **2021**, *143*, 13686−13693.
(46) Annaraj, J.; Suh, Y.; Seo, M. S.; Kim, S. O.; Nam, W. Mononuclear nonheme ferric-peroxo complex in aldehyde deformylation. *Chem. Commun.* **2005**, *36*, 4529−4531.
(47) Corcos, A. R.; Villanueva, O.; Walroth, R. C.; Sharma, S. K.; Bacsa, J.; Lancaster, K. M.; MacBeth, C. E.; Berry, J. F. Oxygen Activation by Co(II) and a Redox Non-Innocent Ligand: Spectroscopic Characterization of a Radical−Co(II)−Superoxide Complex with Divergent Catalytic Reactivity. *J. Am. Chem. Soc.* **2016**, *138*, 1796−1799.
(48) Liu, L.-L.; Li, H.-X.; Wan, L.-M.; Ren, Z.-G.; Wang, H.-F.; Lang, J.-P. A Mn(iii)−superoxo complex of a zwitterionic calix[4]-arene with an unprecedented linear end-on Mn(iii)−O2 arrangement and good catalytic performance for alkene epoxidation. *Chem. Commun.* **2011**, *47*, 11146−11148.
(49) Jesse, K. A.; Anferov, S. W.; Collins, K. A.; Valdez-Moreira, J. A.; Czaikowski, M. E.; Filatov, A. S.; Anderson, J. S. Direct Aerobic Generation of a Ferric Hydroperoxo Intermediate Via a Preorganized Secondary Coordination Sphere. *J. Am. Chem. Soc.* **2021**, *143*, 18121−18130.
(50) McNeece, A. J.; Jesse, K. A.; Xie, J.; Filatov, A. S.; Anderson, J. S. Generation and Oxidative Reactivity of a Ni(II) Superoxo Complex via Ligand-Based Redox Non-Innocence. *J. Am. Chem. Soc.* **2020**, *142*, 10824−10832.
(51) McNeece, A. J.; Jesse, K. A.; Filatov, A. S.; Schneider, J. E.; Anderson, J. S. Catalytic hydrogenation enabled by ligand-based storage of hydrogen. *Chem. Commun.* **2021**, *57*, 3869−3872.
(52) Rudolph, J.; Jacob, C. R. Revisiting the Dependence of Cu K-Edge X-ray Absorption Spectra on Oxidation State and Coordination Environment. *Inorg. Chem.* **2018**, *57*, 10591−10607.
(53) Bair, R. A.; Goddard, W. A. Ab initio studies of the x-ray absorption edge in copper complexes. I. Atomic Cu^{2+} and $Cu(II)Cl_2$. *Phys. Rev. B* **1980**, *22*, 2767−2776.
(54) Tomson, N. C.; Williams, K. D.; Dai, X.; Sproules, S.; DeBeer, S.; Warren, T. H.; Wieghardt, K. Re-evaluating the Cu K pre-edge XAS transition in complexes with covalent metal−ligand interactions. *Chem. Sci.* **2015**, *6*, 2474−2487.
(55) Walroth, R. C.; Uebler, J. W. H.; Lancaster, K. M. Probing CuI in homogeneous catalysis using high-energy-resolution fluorescence-detected X-ray absorption spectroscopy. *Chem. Commun.* **2015**, *51*, 9864−9867.
(56) Sarangi, R. X-ray absorption near-edge spectroscopy in bioinorganic chemistry: Application to M-O(2) systems. *Coord. Chem. Rev.* **2013**, *257*, 459−472.
(57) Donoghue, P. J.; Tehranchi, J.; Cramer, C. J.; Sarangi, R.; Solomon, E. I.; Tolman, W. B. Rapid C−H Bond Activation by a Monocopper(III)−Hydroxide Complex. *J. Am. Chem. Soc.* **2011**, *133*, 17602−17605.
(58) Sarangi, R.; Aboelella, N.; Fujisawa, K.; Tolman, W. B.; Hedman, B.; Hodgson, K. O.; Solomon, E. I. X-ray Absorption Edge Spectroscopy and Computational Studies on LCuO2 Species: Superoxide−CuII versus Peroxide−CuIII Bonding. *J. Am. Chem. Soc.* **2006**, *128*, 8286−8296.
(59) Lim, H.; Thomas, K. E.; Hedman, B.; Hodgson, K. O.; Ghosh, A.; Solomon, E. I. X-ray Absorption Spectroscopy as a Probe of Ligand Noninnocence in Metallocorroles: The Case of Copper Corroles. *Inorg. Chem.* **2019**, *58*, 6722−6730.
(60) DuBois, J. L.; Mukherjee, P.; Stack, T. D. P.; Hedman, B.; Solomon, E. I.; Hodgson, K. O. A Systematic K-edge X-ray Absorption Spectroscopic Study of Cu(III) Sites. *J. Am. Chem. Soc.* **2000**, *122*, 5775−5787.
(61) Meyet, J.; Ashuiev, A.; Noh, G.; Newton, M. A.; Klose, D.; Searles, K.; van Bavel, A. P.; Horton, A. D.; Jeschke, G.; van Bokhoven, J. A.; Copéret, C. Methane-to-Methanol on Mononuclear Copper(II) Sites Supported on Al2O3: Structure of Active Sites from Electron Paramagnetic Resonance. *Angew. Chem., Int. Ed.* **2021**, *60*, 16200−16207.
(62) Zsombor-Pindera, J.; Effaty, F.; Escomel, L.; Patrick, B.; Kennepohl, P.; Ottenwaelder, X. Five Nitrogen Oxidation States from Nitro to Amine: Stabilization and Reactivity of a Metastable

https://doi.org/10.1021/jacs.2c04630
J. Am. Chem. Soc. 2022, 144, 15569−15580

Arylhydroxylamine Complex. *J. Am. Chem. Soc.* **2020**, *142*, 19023−19028.
(63) Liu, Y.; Resch, S. G.; Klawitter, I.; Cutsail, G. E., III; Demeshko, S.; Dechert, S.; Kühn, F. E.; DeBeer, S.; Meyer, F. An Adaptable N-Heterocyclic Carbene Macrocycle Hosting Copper in Three Oxidation States. *Angew. Chem., Int. Ed.* **2020**, *59*, 5696−5705.
(64) Kau, L. S.; Spira-Solomon, D. J.; Penner-Hahn, J. E.; Hodgson, K. O.; Solomon, E. I. X-ray absorption edge determination of the oxidation state and coordination number of copper. Application to the type 3 site in Rhus vernicifera laccase and its reaction with oxygen. *J. Am. Chem. Soc.* **1987**, *109*, 6433−6442.
(65) Mirica, L. M.; Ottenwaelder, X.; Stack, T. D. P. Structure and Spectroscopy of Copper−Dioxygen Complexes. *Chem. Rev.* **2004**, *104*, 1013−1046.
(66) Nakamoto, K. *Infrared and Raman Spectra of Inorganic and Coordination Compounds, Part B: Applications in Coordination, Organometallic, and Bioinorganic Chemistry*; John Wiley & Sons, 2009.
(67) Ginsbach, J. W.; Peterson, R. L.; Cowley, R. E.; Karlin, K. D.; Solomon, E. I. Correlation of the Electronic and Geometric Structures in Mononuclear Copper(II) Superoxide Complexes. *Inorg. Chem.* **2013**, *52*, 12872−12874.
(68) Pirovano, P.; Magherusan, A. M.; McGlynn, C.; Ure, A.; Lynes, A.; McDonald, A. R. Nucleophilic Reactivity of a Copper(II)−Superoxide Complex. *Angew. Chem., Int. Ed.* **2014**, *53*, 5946−5950.
(69) Liu, W.; Twilton, J.; Wei, B.; Lee, M.; Hopkins, M. N.; Bacsa, J.; Stahl, S. S.; Davies, H. M. L. Copper-Catalyzed Oxidation of Hydrazones to Diazo Compounds Using Oxygen as the Terminal Oxidant. *ACS Catal.* **2021**, *11*, 2676−2683.
(70) Ibata, T.; Singh, G. S. Formation of diazoketones and azines by improved oxidation of ketohydrazones using Cu(acac)2 as a catalyst. *Tetrahedron Lett.* **1994**, *35*, 2581−2584.
(71) Żamojć, K.; Zdrowowicz, M.; Rudnicki-Velasquez, P. B.; Krzymiński, K.; Zaborowski, B.; Niedziałkowski, P.; Jacewicz, D.; Chmurzyński, L. The development of 1,3-diphenylisobenzofuran as a highly selective probe for the detection and quantitative determination of hydrogen peroxide. *Free Radical Res.* **2017**, *51*, 38−46.
(72) Iron, M. A.; Szpilman, A. M. Mechanism of the Copper/TEMPO-Catalyzed Aerobic Oxidation of Alcohols. *Chem. - Eur. J.* **2017**, *23*, 1368−1378.
(73) Ryland, B. L.; McCann, S. D.; Brunold, T. C.; Stahl, S. S. Mechanism of Alcohol Oxidation Mediated by Copper(II) and Nitroxyl Radicals. *J. Am. Chem. Soc.* **2014**, *136*, 12166−12173.
(74) Himo, F.; Eriksson, L. A.; Maseras, F.; Siegbahn, P. E. M. Catalytic Mechanism of Galactose Oxidase: A Theoretical Study. *J. Am. Chem. Soc.* **2000**, *122*, 8031−8036.
(75) Liu, J. J.; Diaz, D. E.; Quist, D. A.; Karlin, K. D. Copper(I)-Dioxygen Adducts and Copper Enzyme Mechanisms. *Isr. J. Chem.* **2016**, *56*, 738−755.
(76) Wang, B.; Walton, P. H.; Rovira, C. Molecular Mechanisms of Oxygen Activation and Hydrogen Peroxide Formation in Lytic Polysaccharide Monooxygenases. *ACS Catal.* **2019**, *9*, 4958−4969.
(77) Quek, S. Y.; Debnath, S.; Laxmi, S.; van Gastel, M.; Krämer, T.; England, J. Sterically Stabilized End-On Superoxocopper(II) Complexes and Mechanistic Insights into Their Reactivity with O−H, N−H, and C−H Substrates. *J. Am. Chem. Soc.* **2021**, *143*, 19731−19747.
(78) Peterson, R. L.; Himes, R. A.; Kotani, H.; Suenobu, T.; Tian, L.; Siegler, M. A.; Solomon, E. I.; Fukuzumi, S.; Karlin, K. D. Cupric Superoxo-Mediated Intermolecular C−H Activation Chemistry. *J. Am. Chem. Soc.* **2011**, *133*, 1702−1705.
(79) Kim, S.; Lee, J. Y.; Cowley, R. E.; Ginsbach, J. W.; Siegler, M. A.; Solomon, E. I.; Karlin, K. D. A N3S(thioether)-Ligated CuII-Superoxo with Enhanced Reactivity. *J. Am. Chem. Soc.* **2015**, *137*, 2796−2799.
(80) Klinman, J. P. The Copper-Enzyme Family of Dopamine β-Monooxygenase and Peptidylglycine α-Hydroxylating Monooxygenase: Resolving the Chemical Pathway for Substrate Hydroxylation. *J. Biol. Chem.* **2006**, *281*, 3013−3016.
(81) Stoll, S.; Schweiger, A. EasySpin, a comprehensive software package for spectral simulation and analysis in EPR. *J. Magn. Reson.* **2006**, *178*, 42−55.
(82) Becke, A. D. Density-functional thermochemistry. III. The role of exact exchange. *J. Chem. Phys.* **1993**, *98*, 5648−5652.
(83) Francl, M. M.; Pietro, W. J.; Hehre, W. J.; Binkley, J. S.; Gordon, M. S.; DeFrees, D. J.; Pople, J. A. Self-consistent molecular orbital methods. XXIII. A polarization-type basis set for second-row elements. *J. Chem. Phys.* **1982**, *77*, 3654−3665.
(84) Frisch, M. J. et al.*Gaussian 16*. Revision A.03; Gaussian Inc.: Wallingford CT, 2016.
(85) Gidofalvi, G.; Mazziotti, D. A. Active-space two-electron reduced-density-matrix method: Complete active-space calculations without diagonalization of the N-electron Hamiltonian. *J. Chem. Phys.* **2008**, *129*, No. 134108.
(86) Mazziotti, D. A. Large-Scale Semidefinite Programming for Many-Electron Quantum Mechanics. *Phys. Rev. Lett.* **2011**, *106*, 083001.
(87) Maplesoft, Maple. https://www.maplesoft.com, 2021; Accessed: April 01, 2022.
(88) Maplesoft, Quantum Chemistry Toolbox in Maple. https://www.maplesoft.com, 2021; Accessed: April 01, 2022.
(89) Neese, F. The ORCA program system. *WIREs Comput. Mol. Sci.* **2012**, *2*, 73−78.

https://doi.org/10.1021/jacs.2c04630
J. Am. Chem. Soc. 2022, 144, 15569−15580